

Learning-based prediction of the particles catchment area of deep ocean sediment traps

Théo Picard¹, Jonathan Gula^{2,3}, Ronan Fablet⁴, Jeremy Collin¹, Laurent Mémyer¹

¹Univ Brest, CNRS, IRD, Ifremer, Laboratoire des Sciences de l'Environnement Marin (LEMAR), IUEM, Plouzané, France

²Univ Brest, CNRS, IRD, Ifremer, Laboratoire d'Océanographie Physique et Spatiale (LOPS), IUEM,

Plouzané, France

³Institut Universitaire de France (IUF), Paris, France

⁴IMT Atlantique, Lab-STICC, Plouzané, France

Highlights:

- A Machine learning approach delivers a relevant identification of catchment areas of a sediment trap.
- Numerical simulations suggest that surface data are sufficient to predict the particles' origin.
- Local dynamics affect the prediction performance, which improves in presence of mesoscale vortices and low kinetic energy.

Keywords :

- Biological carbon pump
- Sediment trap
- Machine learning
- Lagrangian particles
- Porcupine Abyssal Plain

24 **Abstract**

25 The ocean biological carbon pump plays a major role in climate and biogeochemical
 26 cycles. Photosynthesis at the surface produces particles that are exported to the deep
 27 ocean by gravity. Sediment traps, which measure the deep carbon fluxes, help to quan-
 28 tify the carbon stored by this process. However, it is challenging to precisely identify the
 29 surface origin of particles trapped thousands of meters deep because of the influence of
 30 ocean circulation on the carbon sinking path. In this study, we conducted a series of nu-
 31 matical Lagrangian experiments in the Porcupine Abyssal Plain region of the North At-
 32 lantic and developed a machine learning approach to predict the surface origin of par-
 33 ticles trapped in a deep sediment trap. Our numerical experiments support its predic-
 34 tive performance, and surface conditions appear to be sufficient to accurately predict the
 35 source area, suggesting a potential application with satellite data. We also identify po-
 36 tential factors that affect the prediction efficiency and we show that the best predictions
 37 are associated with low kinetic energy and the presence of mesoscale eddies above the
 38 trap. This new tool could provide a better link between satellite-derived sea surface ob-
 39 servations and deep sediment trap measurements, ultimately improving our understand-
 40 ing of the biological carbon pump mechanism.

41 **1 Introduction**

42 The Biological carbon pump (BCP) plays a major role in climate and biogeochem-
 43 ical cycles. The BCP reduces unperturbed atmospheric CO₂ by 35% to 50% (Williams
 44 & Follows, 2011) by exporting organic matter to the deep ocean, thereby supporting abyssal
 45 food webs (Billett et al., 1983; Rembauville et al., 2018). The BCP is driven by photo-
 46 synthesis that occurs within the euphotic layer, typically between 0 and 200 meters, pro-
 47 ducing gravitationally sinking particulate organic carbon (POC). Sinking particles have
 48 a wide range of vertical velocities, from neutral buoyancy to more than 600 meters per
 49 day (Villa-Alfageme et al., 2016), and are usually considered to be the main contribu-
 50 tors to the BCP (Armstrong et al., 2001; Alonso-González et al., 2010; Siegel et al., 2014;
 51 F. A. C. Le Moigne, 2019). While most of POC is remineralized in the euphotic and the
 52 mesopelagic zones (200 - 1000 meters), a small but significant fraction of POC reaches
 53 the deep ocean below 1000 m to be sequestered for hundreds or thousands of years (Lampitt
 54 et al., 2008; A. Burd et al., 2016). Despite its critical importance, the annual estimate
 55 of global carbon export remains poorly constrained, ranging from 5 to over 12 Pg C per
 56 year (Turner, 2015). Therefore, quantifying the biological carbon pump is key to under-
 57 standing the global carbon cycle and how the BCP will respond to climate change (Passow
 58 & Carlson, 2012; Henson et al., 2022).

59 Export production has historically been observed with sediment traps (STs) from
 60 the upper thermocline down to several thousand meters (F. A. Le Moigne et al., 2013).
 61 However, linking local primary production to observed exported carbon fluxes is a chal-
 62 lenging task. To effectively interpret ST time series, the catchment area, defined as the
 63 surface domain containing all likely positions from which particles entering the trap could
 64 originate (Deuser et al., 1988), must be clearly identified. Traditionally, the catchment
 65 area is considered to be the zone directly above the traps (Deuser & Ross, 1980; Alldredge
 66 & Gotschalk, 1988; Asper et al., 1992; Armstrong et al., 2001; Lampitt et al., 2023). While
 67 this approach demonstrates a first-order coupling, it is based on a strong hypothesis: the
 68 POC export by gravitational sinking is considered from a quasi one-dimensional (1D)
 69 perspective. However, the ocean circulation significantly affects the particle sinking paths.
 70 Thus, the origin of the particles that reach a deep ST can be distributed over a large do-
 71 main that depends mainly on the ocean dynamics at all scales (Siegel et al., 1990; Deuser
 72 et al., 1990; A. B. Burd et al., 2010; Liu et al., 2018; Dever et al., 2021)

73 Recent studies have focused on the influence of ocean circulation and evaluated fun-
 74 nel statistics for specific sediment trap locations using particle backtracking and numer-

75 ical simulations (Siegel et al., 2008; Liu et al., 2018; Wekerle et al., 2018; Wang et al.,
 76 2022). These studies have shown that the catchment area is highly dependent on sev-
 77 eral factors such as sinking velocities, trap depth, regional and seasonal advective pro-
 78 cesses. The application of Lagrangian backtracking approaches with assimilated ocean
 79 currents has been proposed to relate the ocean circulation to real ST observations (Frigstad
 80 et al., 2015; Ma et al., 2021). However, the full 3D reconstruction of the ocean states from
 81 available satellite-derived and in situ observations is highly challenging and prone to sig-
 82 nificant uncertainties in the retrieval of mesoscale and submesoscale dynamics (Cutolo
 83 et al., 2022). This leads to uncertainties in the prediction of catchment areas and in the
 84 assessment of the BCP.

85 Machine learning tools are increasingly being used to tackle these complex prob-
 86 lems, and generally offer an end-to-end formulation that is easier to develop and com-
 87 putationally cheaper. Oceanography studies have already demonstrated the benefits of
 88 machine learning, particularly in predicting the properties of the ocean interior from ob-
 89 servations of the ocean surface (Chapman & Charantonis, 2017; Bolton & Zanna, 2019;
 90 George et al., 2021; Manucharyan et al., 2021; Pauthenet et al., 2022). They can achieve
 91 state-of-the-art performance or even outperform standard operational interpolation data
 92 assimilation schemes when focused on specific ocean variables (Manucharyan et al., 2021;
 93 Beauchamp et al., 2022; Cutolo et al., 2022). They can also significantly reduce the com-
 94 putational complexity of numerical simulations, including for Lagrangian particle tra-
 95 jectories (Jenkins et al., 2022). It is therefore clear that machine learning offers a wide
 96 range of new possibilities for improving our understanding of the ocean.

97 In this study, we use deep learning schemes to study the catchment areas of deep
 98 ocean particles. Our main contributions are as follows: (i) we formulate the prediction
 99 of the catchment area of particles trapped in STs as the supervised learning of a regres-
 100 sion model from ocean circulation variables; (ii) we investigate whether ocean surface
 101 conditions constrain sinking particles path; (iii) we analyse the main factors affecting the
 102 prediction performance. We report numerical experiments for a case study area in the
 103 North Atlantic using realistic high-resolution simulation data.

104 The paper is organized as follows. Section 2 introduces the methodology use to de-
 105 sign the databases for training and performance evaluation. Section 3 presents the neu-
 106 ral network structure. In section 4, we evaluate the accuracy of the predictions, compare
 107 different configurations and analyse the relationship between input conditions and pre-
 108 diction performance. In Section 5, we discuss potential improvements and future work.
 109 Our conclusions are presented in Section 6.

110 2 Data and case-study area

111 As a case study, we focus on the origin of particles captured by moored ST at the
 112 UK Porcupine Abyssal Plain (PAP) station (49°N , 16.5°W), which provides fluxes with
 113 a temporal coverage of more than 30 years (Hartman et al., 2021). We use a simulation-
 114 based experimental setup consisting of realistic CROCO simulations and particle back-
 115 tracking experiments. More precisely, we simulate particles falling into a fictive PAP ST
 116 located at 1000 m depth, focusing on particles with a vertical sinking velocity of 50 m/day.

117 2.1 Numerical simulation around PAP station

118 We use the realistic North Atlantic Subpolar Gyre simulation designed and vali-
 119 dated by Le Corre et al. (2020). This simulation is run using CROCO (Coastal and Re-
 120 gional Ocean COmmunity model) based on ROMS (Shchepetkin & McWilliams, 2005),
 121 which solves the hydrostatic primitive equations for the momentum and state variables.
 122 The domain has 2000×1600 grid points and a horizontal grid resolution of 2 km, re-
 123 solving the mesoscale and part of the submesoscale. The model has 80 vertical sigma lev-

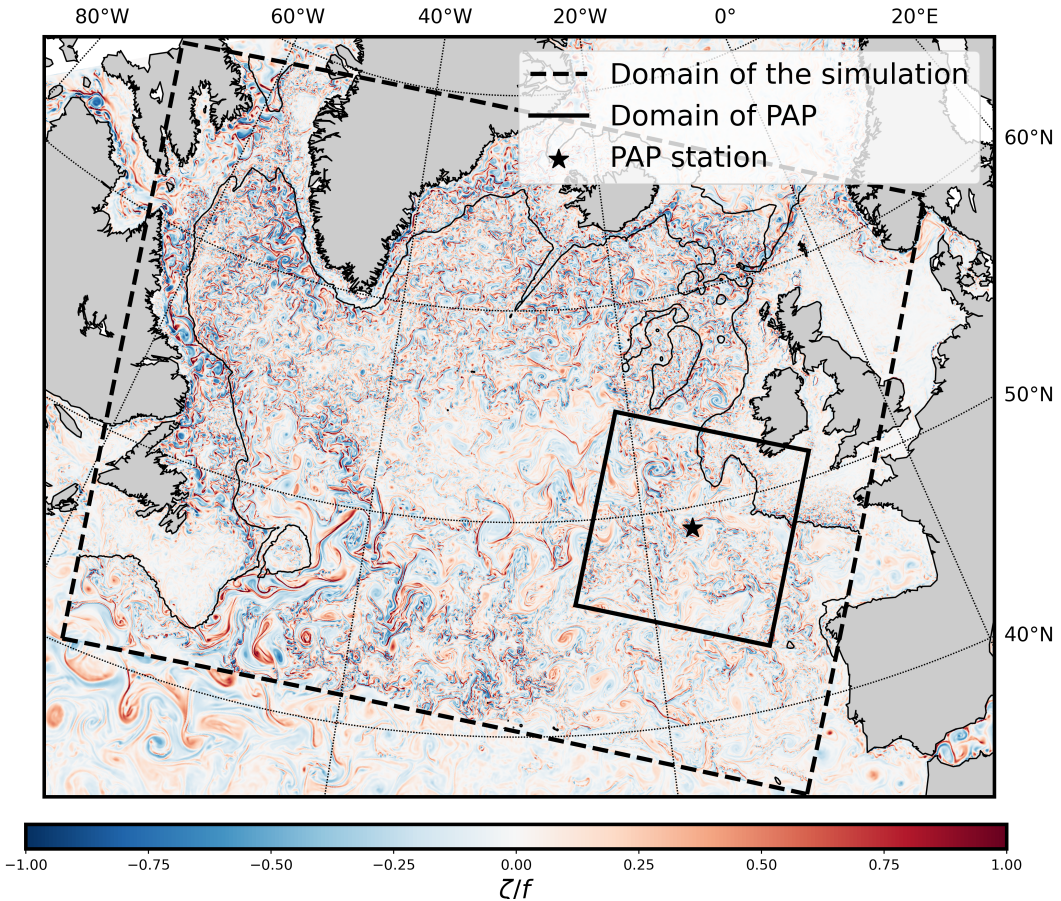


Figure 1. Snapshot of the North Atlantic Subpolar Gyre simulation on 8 February 2008 with relative vorticity. The dashed square is the domain of the simulation. The solid square is the sub-domain we are focusing on. The location of the PAP station is indicated by the black star. The black contour is the bathymetry at 1000 m depth.

els, with a vertical spacing of ~ 5 m at the surface and up to 100 m in the intermediate layer. After a two-year spin-up period, two simulations called POLGYR1 and POLGYR2 are run. POLGYR1 runs between Jan, 1th 2002 and Dec, 4th 2009 (eight years) and is used to create a training and an evaluation database, while POLGYR2 runs between Jul, 24th 2003 and Jan 12nd 2009 (about 6 years and half) and is used for the test database. The two simulation setups are identical in all aspects except for the initial and boundary conditions, which are perturbed in POLGYR2. After spin-up, the chaotic evolution results in uncorrelated dynamics between the two simulations (not shown here). We save snapshots every 12 hours for both simulations. We focus on a 1040×1040 km subdomain centered on PAP station (Figure 1). This region is characterized by moderate kinetic energy compared to the western and northern parts of the subpolar gyre, with a mean flow of about 0.05 m/s (Le Cann, 2005).

2.2 Lagrangian backtracking of catchment areas

A series of Lagrangian experiments are performed offline with Pyticles (Gula & Collin, 2021), using 3d velocities from the POLGYR1/2 simulations. Pyticles is a parallel Fortran/Python Lagrangian tool for offline 3D advection with the ability to include particle behaviour. Transport is performed along the native Arakawa C-grid and terrain-following

141 vertical coordinates of the ocean model. The 3D velocity fields are linearly interpolated
 142 at particles positions, which are advected using a Runge-Kutta 4 numerical scheme. In
 143 addition to passive advection, a negative vertical velocity is applied to simulate the sink-
 144 ing of dense particles. The numerical schemes have been shown to be robust to trajec-
 145 tory reversibility (Wang et al., 2022) using 12-hourly input fields and a time step of 120
 146 seconds.

147 For each experiment, we apply the following procedure. At 1000 m depth, we re-
 148 lease in backtracking 36 particles every 12 hours over a period of 10 days (particle col-
 149 lection period), for a total of 720 particles. The particles are released uniformly over a
 150 patch of 10 km x 10 km and ascend until they reach the base of the euphotic layer at
 151 200 m. Particles have a constant sinking velocity of 50 m/day and their journey takes
 152 on average 15 days, but this can vary from 10 to 20 days (Wang et al., 2022). We save
 153 the particles' positions every 100 m step and compute the resulting Probability Density
 154 Function (PDF). Figure 2a illustrates a typical experiment, in which most of the par-
 155 ticles are attracted to an anticyclone structure visible between 200 m and 1000 m. Bi-
 156 ological particles are mostly created between the surface and 200 m, but we considered
 157 as a first approach that the PDF at 200 m represents the depth from which they are ex-
 158 ported. The PDFs saved at vertical levels lower than 200 m provide information on the
 159 3D+t path of the particles to better constrain the training phase of the network. To im-
 160 prove training efficiency, we also apply a Gaussian filter to each PDF (Figure 2b, c). We
 161 performed sensitivity tests to ensure that increasing the number of particles and the size
 162 of the patch does not significantly affect the PDF. To avoid common particle between
 163 two experiments, we space them 10 days apart. Instead of representing one ST at PAP,
 164 we model 36 STs around the region to increase the number of experiments (Figure 3a
 165). The STs are close enough to the PAP site to have the same hydrodynamical proper-
 166 ties. We choose to space the centres of the patches 36 km apart, so that particles from
 167 two different patches are separated by at least 26 km, which is slightly above the Rossby
 168 radius value in the region (Chelton et al., 1998). This distance is sufficient to observe
 169 significant differences in the catchment areas for two consecutive patches (Figure 3b).

170 For each Lagrangian experiment, we create an output tensor $Y_i = (n_{output} \times \delta x \times$
 171 $\delta y)$, where δx and δy represent the number of points on the horizontal axis and n_{output}
 172 the number of vertical levels where the PDFs are computed. In our case, we consider n_{output}
 173 = 8, corresponding to one layer every 100 m depth from 900 m to 200 m. The hori-
 174 zontal domain was chosen based on the statistical results presented in Wang et al. (2022).
 175 The backtracked particles are distributed within a 800 km x 800 km domain centered
 176 on PAP. Considering a horizontal resolution of 8 km (raw inputs are downsampled for stor-
 177 age constrain), this results in $\delta y = \delta x = 100$ points. For each output Y_i , we store a
 178 corresponding input tensor $X_i = (n_{input} \times \delta x \times \delta y)$ which contains the hydrodynamic
 179 conditions of the experiment i . These data include temperature, vorticity, horizontal ve-
 180 locities (u and v), and sea surface height (SSH). All the variables are extracted on the
 181 same horizontal domain as Y_i and downsampled to a resolution of 8 km. To capture the
 182 temporal variability, we consider a 10-day time sampling over a 30-day time window (4
 183 time steps). To evaluate the importance of the surface in comparison to the sub-surface
 184 data (Section 4), we distinguish two datasets, $D_{4layers}$ and D_{surf} :

- 185 • $D_{4levels}$: this dataset contains the variables at 4 vertical levels, i.e. surface, 200
 186 m, 500 m, 1000 m. Each input tensor is a $68 \times 100 \times 100$ -dimensional tensor, where
 187 $n_{input} = 68$ represents the number of input fields extracted for each experiment.
- 188 • D_{surf} : This dataset contains only sea surface conditions. This results in $20 \times 100 \times$
 189 100-dimensional input tensors.

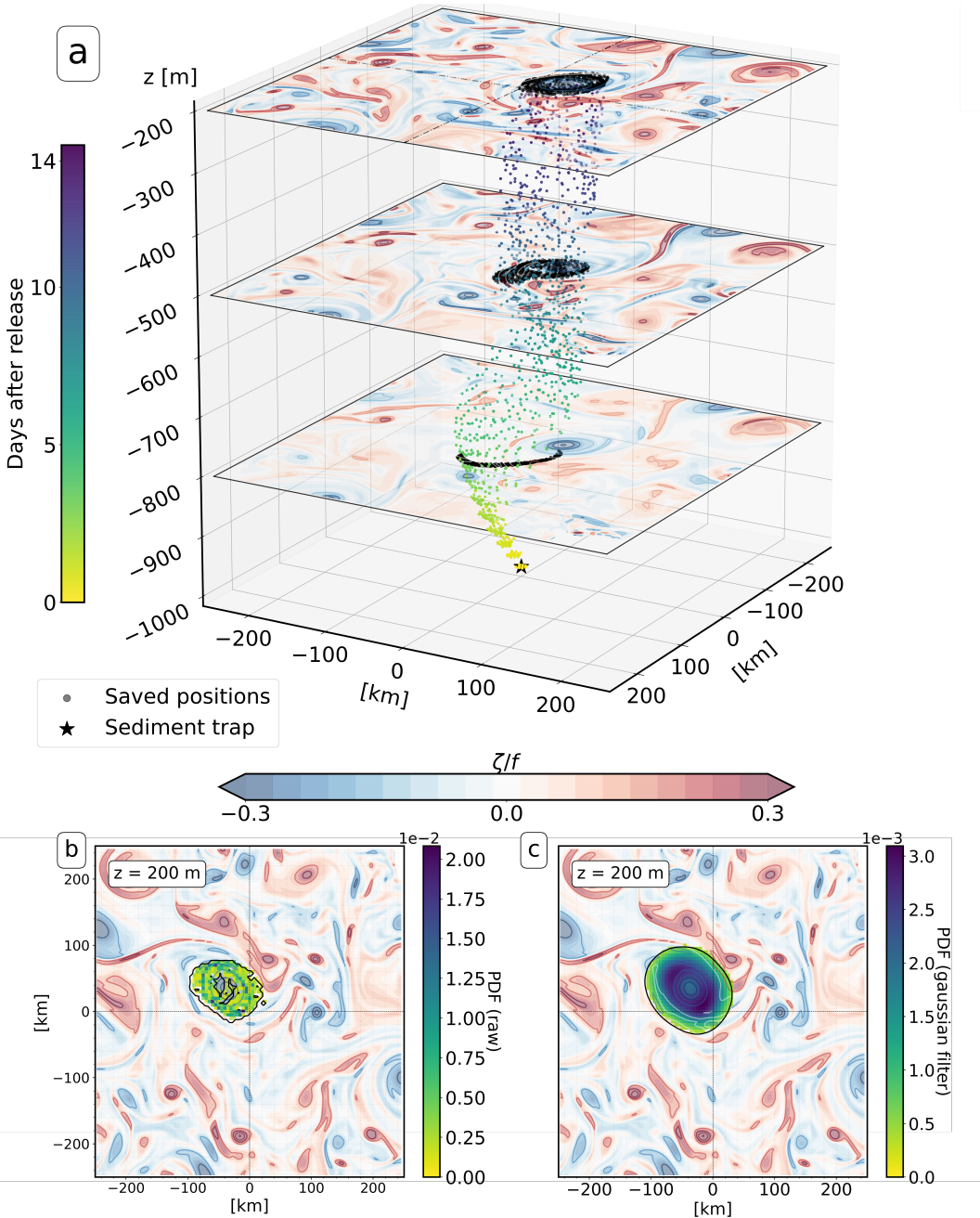


Figure 2. a) 3D view of the Lagrangian experiment. The color of the particles represents the number of days after their release at the ST (5% of particles are plotted). Snapshots of relative vorticity are displayed at 3 vertical layers (-800 m, -500 m, -200 m). Black points on the visualization indicate all the saved positions of particles at these specific vertical levels. b) The computed raw PDF of particles at 200 m c) PDF at 200 m after the Gaussian filter.

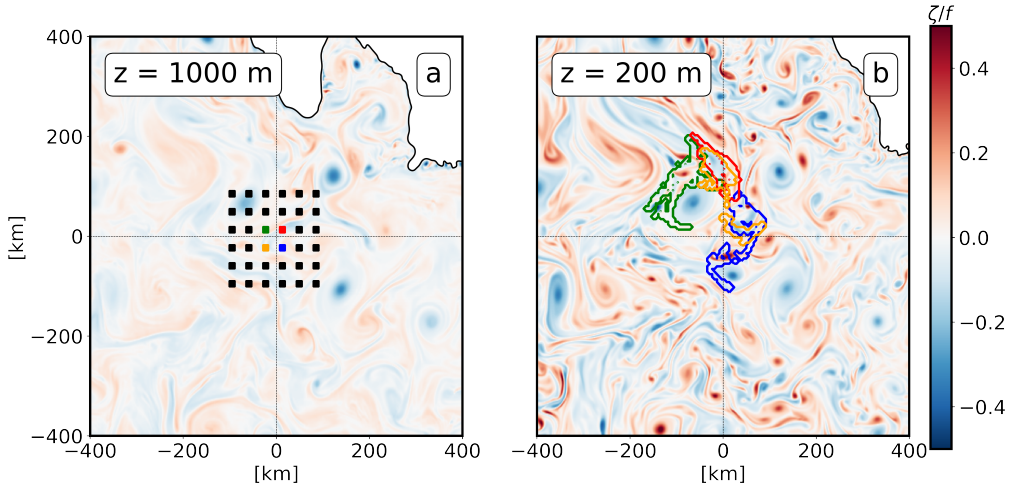


Figure 3. Snapshots of the relative vorticity on Oct 22 2003 (POLGYR1), 20 days after the particle release. a) vorticity field at a 1000 m depth with the 36 initial positions of the particles (black and colored squares). b) vorticity field at a 200 m depth with superimposed the origins of the backtracked particles for the 4 colored patches of the left panel.

3 Proposed deep learning scheme

This section introduces the proposed deep learning scheme, in particular the proposed neural architecture and the training scheme.

3.1 Training, validation and test data

Following the training and evaluation frameworks used in deep learning studies (Lecun et al., 2015), we consider independent training, validation and test datasets as follows. With the Lagrangian experiments presented above, we create a training and a validation dataset using the first simulation setup POLGYR1 (2002 to 2008) and obtain a total of 10260 samples. We divide the samples into a training database (8604 samples from January 2002 to September 2008) and an evaluation database (1224 samples from year 2009). Note that data from September 2008 to January 2009 are not used. The two datasets are separated by a 100-day period to ensure statistical independence. For the test dataset, 6800 samples are created with POLGYR2. They are independant of the training and evaluation experiments.

3.2 Architecture

As shown in Figure 4, we use a U-net architecture type (Ronneberger et al., 2015). The U-Net is a state-of-the-art neural architecture for a wide range of image-to-image mapping tasks, including application to ocean studies (Barth et al., 2020; Beauchamp et al., 2022).

The input to the network stacks the hydrodynamic conditions and a $8 \times 100 \times 100$ -dimensional tensor representing the initial PDF of the particles. All the initial PDFs have probability of 0.25 over the 4 points in the center of the map, representing the release patch (not shown). The network consists of a series of convolutional (kernel = 5), ReLu and Batch norm layers. A 3-step pooling process allows the resolution to be progressive downsampled from 8 km to 32 km. Combining these steps with skip connections enables

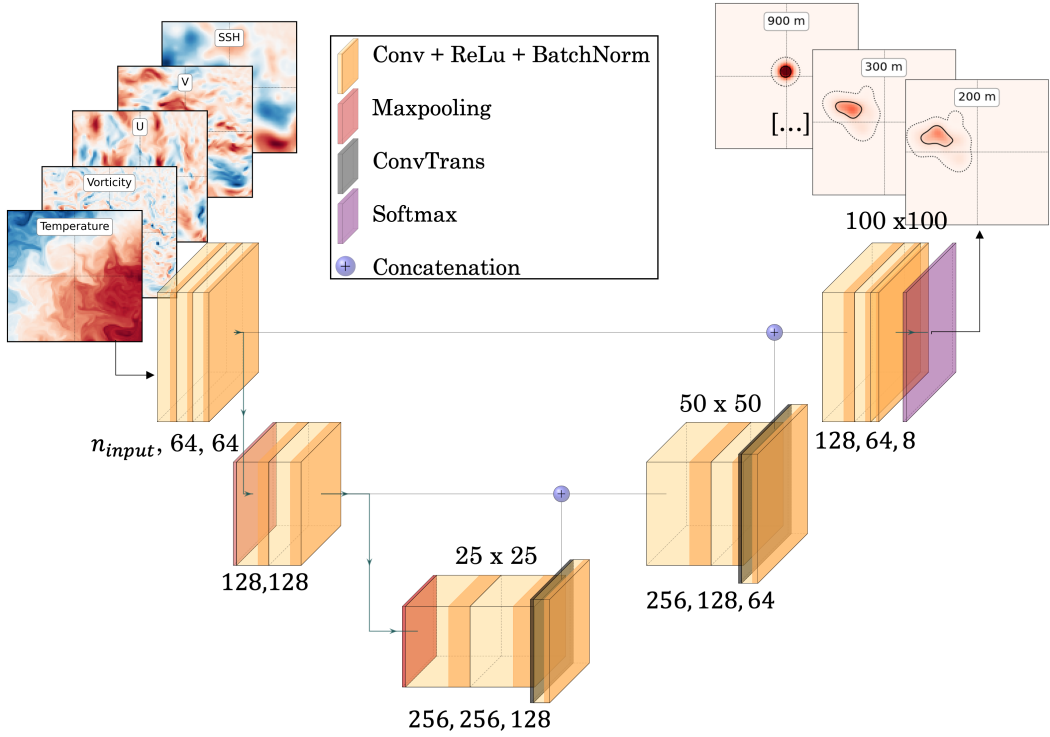


Figure 4. General architecture of the Unet. The inputs are temperature, vorticity, u , v , and ssh images at multiple time steps and depths concatenated with initial PDFs (not shown). The outputs are the PDFs at 8 depths representing the funnel of the particles. At the top of each layer we show the resolution of the images and at the bottom the number of channels.

the detection of hydrodynamic structures at different spatial scales. The final layer of the U-Net is a softmax layer to provide normalized PDF predictions. The output of the network is a $8 \times 100 \times 100$ -dimensional tensor composed of the predicted PDFs from 900 m to 200 m (every 100 m). The last PDF at 200 m represents the predicted origin of the particles.

3.3 Training scheme

As training criterion, we consider the Bhattacharyya coefficient (Bhattacharyya, 1943) to assess how well the predicted PDFs match the real ones. The Bhattacharyya coefficient provides a similarity score between two PDFs, and leads to the Bhattacharyya training loss (BL):

$$BL = 1 - BC = 1 - \sum \sqrt{P_i Q_i}$$

where P_i is the predicted probability at point i and Q_i is the true probability at the same point. BL ranges from 1 to 0, with 0 representing a perfect prediction. During the training phase, we aim to minimize the following loss function (L) :

$$\mathcal{L} = \frac{BL_{200m} + BL_{300m} + \dots + BL_{800m} + BL_{900m}}{n_{layer}}$$

L is the mean of the BL computed at each of the 8 vertical layers. The aim is to force the model to consider the evolution of particles along the water column. Empirically, this method improves the performance of the trained model compared to experiments where the training loss is based only on BL_{200m} .

We implement our deep learning scheme using PyTorch (Paszke et al., 2019). For the training phase, the Adam optimization algorithm (Kingma & Ba, 2015) is used with the following hyperparameters: $\beta = (0.5, 0.999)$, no weight decay, and a learning rate of 0.001. The training process is performed using mini-batches of size 32. After 50 training epochs, the best model is selected based on its performance on the evaluation data. We further improve the performance and robustness of the model by using a bootstrapping method with 10 replicates (Breiman, 1996). The final prediction is a set of PDFs computed as the median of the predictions from the 10 models, followed by re-normalization step. We also compute the standard deviation of the 10 predictions as a confidence index (see section 5).

4 Results

We report the numerical experiments performed on the considered PAP case study. First, we detail a benchmarking experiment to evaluate the performance of the proposed deep learning schemes. Second, we further analyse how the hydrodynamic conditions affect the prediction performance.

4.1 Prediction performance and comparison

We evaluate the performance of several models on the test database using the BL_{200m} metric (i.e. the Bhattacharyya distance between the predicted PDF and the true PDF for the catchment area at 200m depth). After a visual analysis of the predictions and associated scores, we set up the following evaluation criterion. We consider a prediction to be valid if $BL \leq 0.2$, and not valid if $BL < 0.3$. For predictions with a value of BL between 0.2 and 0.3, the global area is often still well predicted, but the values of the PDF are usually rough. In these cases, we decide to create a third class called "quasi-valid". These predictions are not considered valid, but still provide valuable information in the search for particle origins, and this information needs to be highlighted in the final score statistics.

We benchmark different models in Table 1. The $Unet_{4layers}$ model is the U-net presented in section 3, trained and tested with the $D_{4layers}$ database, which contains both surface and sub-surface information. The $Unet_{surf}$ model uses only surface information from the D_{surf} database. $Unet_{surf-nb}$ is similar to $Unet_{surf}$ but without the use of the bootstrap method. The $CNN_{surf-basic}$ model includes a simple CNN architecture consisting of a series of convolutional layers with a Relu activation function, which we tested with D_{surf} . We also include a *Baseline* prediction given by the average of all the true PDFs used in the training database. This mean PDF roughly corresponds to a 2D Gaussian distribution centred on PAP, as also presented in Wang et al. (2022).

The *Baseline* and $CNN_{surf-basic}$ models have poor performance with 0 valid cases. This highlights the complexity of the prediction task and the need for non-trivial models. It is noteworthy that the U-net architecture seems to be well suited to this problem. $Unet_{surf-nb}$ achieved a very good performance of 58 % of valid cases, which was increased to 66% with the use of bootstrapping. Taking into account the quasi-valid predictions, $\sim 85\%$ of the predictions provide valuable information with only surface data. However, the comparison between $Unet_{4layers}$ and $Unet_{surf}$ demonstrates the importance of sub-surface information to obtain more accurate and robust predictions. With 81 % of valid cases and 13 % of quasi-valid cases, $Unet_{4layers}$ clearly outperforms $Unet_{surf}$. This would mean that in about 10-15% of the cases, subsurface data is required to make valid predictions. Figure 5 shows examples of predictions from the test database using the $Unet_{4layers}$ and $Unet_{surface}$ models. The PDF is represented by two contours, one containing 99% of the particles (dotted contour) and the other containing 50% of the particles (solid contour). Both models have a good ability to predict the overall catchment area. However, valid predictions are mainly characterised by a well predicted center of the PDF, which

Table 1. Score and performance for different model architectures. For each model we indicate the number of parameters (nb param), the averaged prediction score BL_{200m} , the percentage of valid, quasi-valid and non-valid test cases.

Models	Nb param	BL_{200m}	Valid prediction [%]	Quasi-valid prediction [%]	Non-valid prediction [%]
$Unet_{4layers}$	1.9M (x10)	0.13	81	13	6
$Unet_{surf}$	1.8M (x10)	0.18	66	19	15
$Unet_{surf-nb}$	1.8M	0.21	58	23	20
$CNN_{surf-basic}$	205K	0.61	0	1	99
<i>Baseline</i>	0	0.45	0	8	92

is usually more accurate for $Unet_{4layers}$. In the following, we only focus on $Unet_{4layers}$ and $Unet_{surface}$ predictions.

4.2 Statistical analyse of the performance

We quantitatively analyze potential causes of valid or invalid predictions. The examples show that the shape of the particle distributions has a significant impact on score prediction. We find that PDF far from the ST with mass center > 150 km (i.e the average distance of the particles from their source) are generally not well predicted (Figure 5 and Table 2, index 16, 21, 25). Similarly, complex PDF shapes characterised by multiple patches spread across the domain (index n°2, 15, 16 in Figure 5) appear difficult to predict. The entropy ($-\sum p_i \log(p_i)$, where p_i is the PDF value at point i) characterises the complexity of the PDF beyond its variance. The entropy increases with the spread of particles and for multimodal distributions and high entropy value (> 6.6) could explain in some cases the prediction bias (Table 1 index 2, 15, 16). This trend is confirmed by the statistical analysis over the whole test dataset shown in Figure 6. With a mass center above 200 km, the chance of having a valid prediction with $Unet_{surf}$ is less than 30%. Similarly, we observe a trend of progressive degradation of the score for PDFs with an entropy higher than 6.6 (Figure 6b).

Several physical factors could be responsible for the final PDF shape. To characterise the local dynamics, we choose to compute the Mean Kinetic Energy (MKE) and the Eddy Kinetic Energy (EKE) around the ST such as:

$$\underbrace{\frac{1}{2}(\bar{u}^2 + \bar{v}^2)}_{KE} = \underbrace{\frac{1}{2}(\bar{u}^2 + \bar{v}^2)}_{MKE} + \underbrace{\frac{1}{2}(u'^2 + v'^2)}_{EKE} \quad (1)$$

where u and v are the two components of the horizontal ocean velocity, \bar{u} and \bar{v} are the velocities averaged over a 30-day window, corresponding to the characteristic time of our Lagrangian experiments. Finally, u' and v' are defined as follows:

$$u' = u - \bar{u} \quad (2)$$

$$v' = v - \bar{v} \quad (3)$$

MKE and EKE are spatially averaged within a 400 km box around the ST, and vertically between 200 m and 1000 m. These averages are computed every 10 days. MKE can

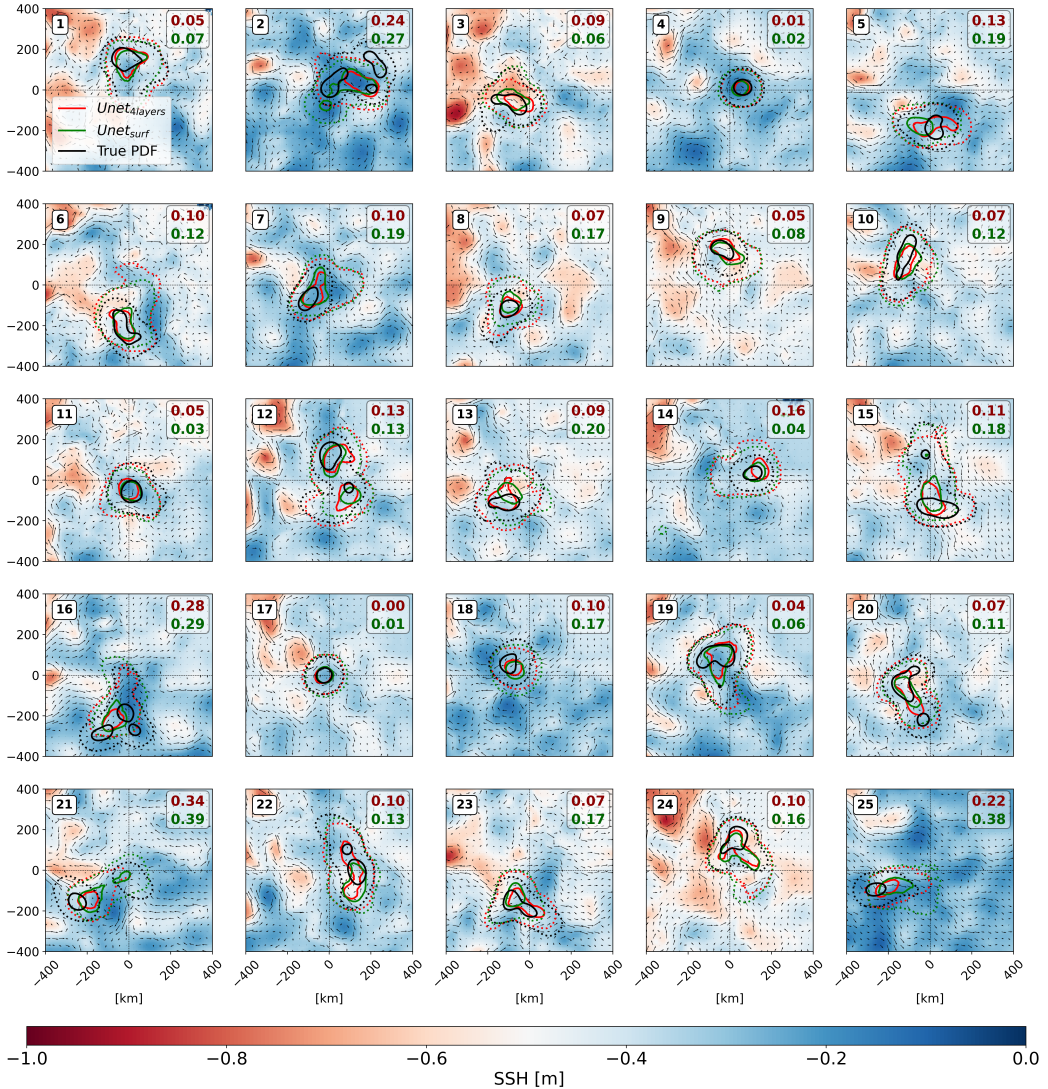


Figure 5. Examples of predictions. PDFs predicted with $Unet_{4\text{layers}}$ (red) and with $Unet_{surf}$ (green). Black contours represent the true origins of particles. Dotted contours contain 99 % of the particles, solid contours contain 50 %. $BL_{200\text{m}}$ score is given for both predictions on the top right. On the background : snapshot of SSH at day +20 after the first particle release with the surface velocities represented with the arrows. All domain size are 800 x 800 km and centered on the trap where particles are released.

Index	BL_{200m}^{surf}	BL_{200m}^{4L}	Mass center	Entropy	MKE	EKE	$\zeta/f_{10^{-2}}$	$OW/f_{10^{-3}}$
10th per	0,06	0,04	36	5,7	69	32	-4,1	-1,4
50th per	0,15	0,11	99	6,3	95	49	-0,4	2,2
90th per	0,35	0,26	193	6,7	126	71	3,6	12,1
1	0,07	0,05	136	6,5	90	81	-4,6	7,4
2	0,27	0,24	136	6,9	94	65	-2,4	2,0
3	0,06	0,09	110	6,4	101	82	4,2	-1,1
4	0,02	0,01	63	5,7	124	31	-4,9	-2,6
5	0,19	0,13	183	6,1	127	46	0,9	4,0
6	0,12	0,10	216	6,4	107	50	-0,4	-0,7
7	0,19	0,10	109	6,0	96	44	-4,4	-2,0
8	0,17	0,07	164	5,9	98	57	0,8	3,3
9	0,08	0,05	172	6,0	82	39	3,0	7,9
10	0,12	0,07	178	6,3	79	47	3,2	1,3
11	0,03	0,05	62	6,2	89	58	-5,1	4,6
12	0,13	0,13	51	6,7	65	47	-2,4	1,1
13	0,20	0,09	148	6,4	74	39	2,2	0,8
14	0,04	0,16	114	5,6	84	36	1,1	1,7
15	0,18	0,11	68	6,8	114	38	1,8	3,0
16	0,29	0,28	242	6,6	91	53	-3,7	0,9
17	0,01	0,00	24	5,5	131	36	-5,0	-2,2
18	0,17	0,10	110	5,9	60	41	1,7	0,3
19	0,06	0,04	95	6,7	137	45	-2,5	2,6
20	0,11	0,07	133	6,7	85	31	2,2	3,8
21	0,39	0,34	257	6,0	89	51	-1,1	2,0
22	0,13	0,10	114	6,5	89	32	-1,0	4,4
23	0,17	0,07	181	6,4	98	35	0,2	0,3
24	0,16	0,10	140	6,3	132	40	-1,8	20,6
25	0,38	0,22	270	5,7	92	27	0,6	0,3

Table 2. Variables associated to the Lagrangian experiments. BL_{200m}^{surf} and BL_{200m}^{4L} indicates the Bhattacharya loss at 200m for surface and 4L model. We computed the PDFs' mass center [m] and entropy. The MKE and EKE [$cm^2.s^{-2}$] are computed with a temporal window of 30 days (period of the Lagrangian experiment) and averaged between 200 m and 1000 m in a 400 km box centred at the ST. ζ/f and OW/f are computed from a surface snapshot taken 20 days after the first particle release and averaged inside a 100 km box centred at the ST. The values of the median, 10th percentile and 90th percentile are given at the top. Index number correspond to the examples given Figure 5.

be associated with large-scale currents and mesoscale eddies that stay stable during the time window. A large MKE implies strong velocities that are likely to transport the particles far from their source, further complicating the prediction process. EKE typically indicates the presence of moving mesoscale eddies or submesoscale fronts. These smaller scale dynamics can promote divergent flows and increase the entropy, thus affecting the prediction score.

The number of invalid predictions increases on average with both MKE and EKE (Figure 6c, d), although the relationship between the prediction and EKE/MKE is not always simple when looking at all the cases in Table 2. Moreover, the influence of MKE seems to explain the seasonal patterns we observe with the 5-year temporal coverage (Figure 7). For both *Unet* models, the best performance was achieved in winter/early spring, while the highest probability of a non-valid prediction was observed in summer. We found a strong correlation ($r^2 = 0.64$) between this trend and the seasonal evolution of MKE. This observation leads us to suggest that MKE could be the main driver of the score on long time scales. The EKE evolution shows a weaker correlation ($r^2 = 0.13$). In particular, the EKE peak visible in April, associated with the deepest mixed-layer and intensified submesoscale activity down to 500 m Buckingham2016, is not clearly reflected in the performance score.

However, Table 2 suggests that MKE and EKE are not sufficient to explain the prediction score in all cases. The presence of coherent vorticity structures above the trap appears to facilitate the prediction (5 index 4, 11, 17). To demonstrate this, we analyze dynamical features using three indicators: the surface relative vorticity $\zeta = v_x - u_y$, the Okubo-Weiss parameter $OW = \sigma^2 - \zeta^2$ with $\sigma = (u_x - v_y) + (v_x + u_y)$ and the sea level anomaly $SLA = SSH - <SSH>$ where $<SSH>$ is the averaged SSH within the subdomain. All these variables are taken from a surface snapshot on the 20th day after the first release and averaged within a $100 \text{ km} \times 100 \text{ km}$ area centered on the ST (Figure 6e, f, g and Table 2). The best performances (> 80% of valid predictions) are associated with low negative OW, high absolute ζ and SLA. This situation generally corresponds to the presence of a vortex structure above the trap (Wang et al., 2022). On the other hand, the chaotic situations that can be described by $OW > 0$, $\zeta \sim 0$, and $SLA \sim 0$ are generally associated with the worst performance.

The presence of large scale currents and eddies appears to be sufficient to explain the prediction scores to a first order approximation: Large KE is typically associated with lower scores, unless we have coherent structures above the trap (corresponding to large KE with negative OW and large vorticity amplitudes). This is highlighted by the bin statistics in Figure 8. The 'non-valid' prediction area in Figure 8a is defined by $KE > 160 \text{ cm}^2 \cdot \text{s}^{-2}$ and $|\zeta/f| < 0.05$, and is characterized by an averaged Bhattacharyya score greater than 0.2 (indicated by the red bins). Similarly, it is possible to observe the same 'non-valid' prediction zone in Figure 8b, defined by $KE > 160 \text{ cm}^2 \cdot \text{s}^{-2}$ and $OW/f > -0.0075$.

5 Discussion

In this section, we discuss the possible interpretations of the results, present the limitations of the model, and explore potential improvements that will guide our future work.

5.1 Interpretation of statistics and confidence index

Our results support the relevance of the proposed machine learning approach to predict the catchment area of particles using only surface data. Although subsurface information can improve the quality of the prediction, it is not essential in most cases. Analysis of the drivers of the prediction score revealed complex multifactorial causes. Only

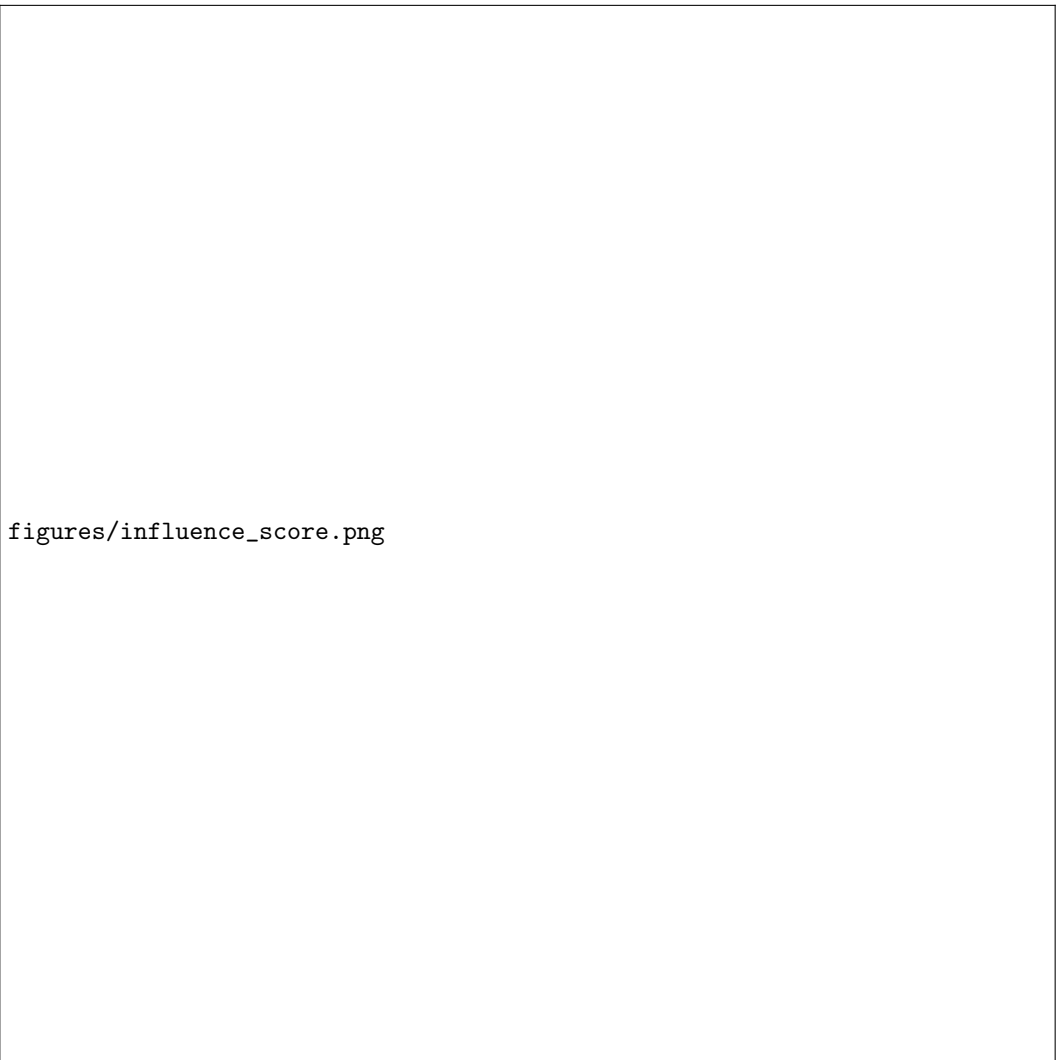


Figure 6. Fraction of non-valid prediction ($BL_{200m} > 0.2$) depending on local dynamical variables a) PDF mass center shift, b) PDF Shannon entropy $-\Sigma p \log(p)$, c) Eddy Kinetic Energy (EKE), d) Mean Kinetic Energy (MKE), e) relative surface vorticity ζ/f , g) Surface relative Okubo-Weiss OW/ f^2 , g) Sea Level Anomaly (SLA), and h) standard deviation (STD) of the 10 bootstrap models. For c and d, the energy is averaged in a 400 km box centred on the ST and between 200 and 1000 m. A temporal averaging window of 30 days is used for MKE and EKE. For e, f, g the local dynamical variables come from surface snapshot taken 20 days after the first particle release and averaged in a 100 km box around the ST.

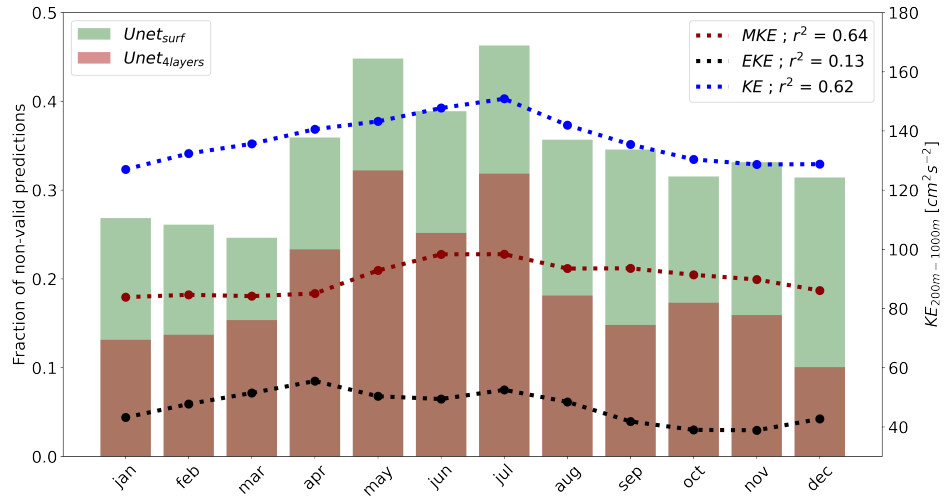


Figure 7. Monthly performance statistics over the testing period for *Unet_{surf}* and *Unet_{4layer}*. Bar score indicate the probability of non-valid prediction ($BL_{200m} > 0.2$). The monthly averaged evolution of EKE (dotted) and MKE (dashed) between 200 and 1000 m is shown in black.

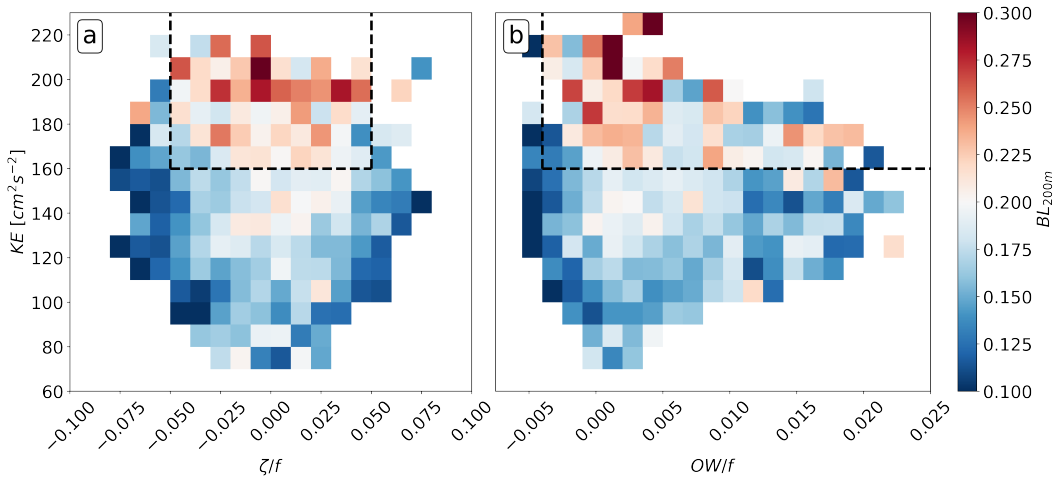


Figure 8. Averaged bin statistics of the prediction score in the a) Kinetic Energy - relative vorticity space b) Kinetic Energy - relative Okubo-Weiss space. Color represents the mean Bhattacharyya score. Bins with less than 5 samples inside are masked. The dashed black lines delimit the "non-valid" prediction zone represented by the red bins.

a few indicators have been chosen for this analysis, and we do not exclude the possibility of other links that have not been investigated. However, the statistics appear coherent to us, as they suggest that the model is more robust under weak and/or stable dynamics. Given that our model is limited in time and space by the input resolution (8 km resolution, only surface or 4 vertical layers and snapshots every 10 days), it is clear that the predictions are sensitive to finer spatial and temporal variability. This may explain the good performance with small KE or in the presence of coherent eddies above the trap. Eddy structures can have a clear surface signature that is easy to identify and that stay coherent at depth (Figure 2). Considering a 30-day period, they are generally stable showing little temporal variability, limiting the particles' spatial dispersion trapped inside. In contrast, chaotic situations, typically characterized by randomly distributed submesoscale fronts with a horizontal size of about 10 km, are more likely to be less well predicted. Additionally, such structures can be too small to be detected. Temporal evolution can be very fast (on the order of days) and is unlikely to be adequately captured by our machine learning models. Such assumptions can directly help in the future to develop a confidence index that depends on the local dynamics. For future real applications, it will probably be difficult to predict the catchment area in every situation. The aim is therefore to understand in which situation the predictions made by the machine learning model can be trusted. In this respect, the standard deviation (STD) of the 10 model predictions from the bootstrap method (Figure 6f) can also provide insight into quantifying the uncertainties of the predictions. The STD, computed as the mean STD of the 10 models at each prediction point, shows a linear relationship with the probability of having a valid prediction for the Unet models. Previous studies have also explored such bootstrapping methods for uncertainty quantification (Pauthenet et al., 2022; Beauchamp et al., 2022; Haynes et al., 2023). Future work could also explore more advanced deep learning schemes with built-in uncertainty quantification properties (Haynes et al., 2023).

377 5.2 Towards real data and a more realistic representation of particles

378 The results strongly suggest a possible use of satellite data to more precisely identify
 379 the source area of the particles measured in the deep ocean. As emphasized by Fevre
 380 et al. (in prep) for the learning-based mapping of sea surface dynamics, the represen-
 381 tativeness of the numerical simulations w.r.t. the real 3D + T hydrodynamic conditions
 382 is likely to be a critical feature for the application of a neural model trained from sim-
 383 ulation data to a real-world configuration. The use of ocean reanalyses (Frigstad et al.,
 384 2015) could also be a relevant solution. In both cases, an in-depth analysis of the 3D ocean
 385 circulation seems particularly important to assess the potential limitations of the pro-
 386 posed scheme.

387 Regarding biology, we consider a ST at 1000 m, whereas in reality the ST at PAP
 388 are moored deeper (~ 3000 m). It has been shown that below 1000 m, currents are weaker
 389 and do not significantly affect the horizontal displacement of particles (Wang et al., 2022).
 390 Therefore, although the influence of ST depth on the prediction score needs to be inves-
 391 tigated, it can be assumed that it will not significantly affect the model performance. How-
 392 ever, a major bias in the model probably comes from the carbon particle representation.
 393 We represent sinking particles with a settling velocity of 50 m/day, whereas particles have
 394 a wide range of velocities that can vary significantly seasonally (Villa-Alfageme et al.,
 395 2016). The origin of particles can be very different depending on their sinking velocity,
 396 so it is important to consider the whole particle velocity spectrum to represent the catch-
 397 ment areas for particles with different velocities (Wekerle et al., 2018). Therefore, the
 398 next step of this study is to focus on the effect of sinking velocities on the prediction score.
 399 We can assume that the prediction of catchment areas for particles with higher speeds
 400 than 50 m/day is likely to be more efficient, as their trajectories are less impacted by
 401 currents and turbulence (Liu et al., 2018; Wekerle et al., 2018; Ma et al., 2021; Wang et
 402 al., 2022). However, particles with lower sinking velocities are more sensitive to the flow

403 and can easily be dispersed over a large area far away from the ST, which would decrease
 404 the prediction score, as suggested in Figures 6b and d.

405 The use of a coupled biogeochemical model embedded in POLGYR would provide
 406 information on surface chlorophyll distribution (i.e. sea colour) and primary production
 407 intensity (PP) (Kostadinov et al., 2009; Dunne et al., 2005). Although the relationships
 408 are not direct (Laurenceau-Cornec et al., 2020; Iversen & Lampitt, 2020; Cael et al., 2021),
 409 high PP levels are associated with large phytoplankton cells and particles, which may
 410 be associated with higher sink rates. It is then possible to weigh the distribution of par-
 411 ticles in terms of size and sinking velocity against the PP estimated by the model where
 412 they are exported, which should make the simulations more realistic. In addition, sea
 413 colour observations, together with altimetry data, can be used as input to a machine learn-
 414 ing system to better constrain carbon fluxes at depth, using an approach similar to that
 415 presented here. However, particle size and sinking velocity are affected by numerous bi-
 416 ological processes during their journey, which are generally not taken into account in sim-
 417 ple Lagrangian studies. Although a Lagrangian approach can be developed (Jokulsdottir
 418 & Archer, 2016), an ad hoc parameterisation, for example derived from BGC models sim-
 419 ulating particle dynamics (Aumont et al., 2015), could also be used and tested.

420 6 Conclusion

421 Identifying the origin of particles captured by sediment traps is important for in-
 422 terpreting measured fluxes and improving sampling methods. This task is challenging
 423 and often leads to inaccurate assumptions or requires complex 3D data assimilation mod-
 424 els. In our study, (i) we demonstrate the ability of machine learning to predict the ori-
 425 gin of particles trapped in a PAP sediment trap in real time, based on realistic 3D nu-
 426 matical simulation and Lagrangian tracking. (ii) We found that the catchment area of
 427 particles is mainly driven by ocean surface conditions, suggesting that our machine learn-
 428 ing model could be applied to satellite data. (iii) Statistical analysis shows that the per-
 429 formance of the prediction is sensitive to local dynamics. The model performs better at
 430 low KE and in the presence of coherent vortices above the sediment trap. The next chal-
 431 lenge is to apply our model to real data and develop a confidence index based on the lo-
 432 cal conditions. The particle modeling also needs to be improved to account for the wide
 433 range of particle sinking velocities.

434 **Acknowledgments**

435 T.P. received a Ph.D. grant from École Normale Supérieure Paris-Saclay. This work
 436 was also supported by the ISblue project, an Interdisciplinary graduate school for the
 437 blue planet (ANR-17-EURE-0015), and co-funded by a grant from the French govern-
 438 ment under the program "Investissements d'Avenir". This manuscript contributes to the
 439 APERO project funded by the National Research Agency under the grant APERO [grant
 440 number ANR ANR-21-CE01-0027] and by the French LEFE-Cyber program. Simula-
 441 tions were performed using HPC resources from GENCI-TGCC (grant 2018-A0050107638)
 442 and from DATARMOR of "Pôle de Calcul Intensif pour la Mer" at Ifremer, Brest, France.
 443 J.G. would like to acknowledge support from the French National Agency for Research
 444 (ANR) through the project DEEPER (ANR-19-CE01-0002-01) and AI chair OceaniX
 445 (ANR-19-CHIA-0016). Simulations were performed using HPC resources from GENCI-
 446 TGCC (Grants 2022-A0090112051), and from HPC facilities DATARMOR of "Pôle de
 447 Calcul Intensif pour la Mer" at Ifremer Brest France. The authors thank Mathieu Le
 448 Corre for providing CROCO simulation outputs.

449 **References**

- 450 Alldredge, A. L., & Gotschalk, C. (1988). In situ settling behavior of marine snow.
 451 *Limnology and Oceanography*, 33(3). doi: 10.4319/lo.1988.33.3.0339
- 452 Alonso-González, I. J., Arístegui, J., Lee, C., & Calafat, A. (2010). Regional
 453 and temporal variability of sinking organic matter in the subtropical north-
 454 east Atlantic Ocean: A biomarker diagnosis. *Biogeosciences*, 7(7). doi:
 455 10.5194/bg-7-2101-2010
- 456 Armstrong, R. A., Lee, C., Hedges, J. I., Honjo, S., & Wakeham, S. G. (2001).
 457 A new, mechanistic model for organic carbon fluxes in the ocean based
 458 on the quantitative association of POC with ballast minerals. *Deep-
 459 Sea Research Part II: Topical Studies in Oceanography*, 49(1-3). doi:
 460 10.1016/S0967-0645(01)00101-1
- 461 Asper, V. L., Deuser, W. G., Knauer, G. A., & Lohrenz, S. E. (1992). Rapid cou-
 462 pling of sinking particle fluxes between surface and deep ocean waters. *Nature*,
 463 357(6380). doi: 10.1038/357670a0
- 464 Aumont, O., Ethé, C., Tagliabue, A., Bopp, L., & Gehlen, M. (2015, aug). PISCES-
 465 v2: An ocean biogeochemical model for carbon and ecosystem studies. *Geosci-
 466 entific Model Development*, 8(8), 2465–2513. doi: 10.5194/gmd-8-2465-2015
- 467 Barth, A., Alvera-Azcárate, A., Licer, M., & Beckers, J.-M. (2020). DINCAE 1.0:
 468 a convolutional neural network with error estimates to reconstruct sea surface
 469 temperature satellite observations. *Geoscientific Model Development*, 13(3),
 470 1609–1622. Retrieved from <https://gmd.copernicus.org/articles/13/1609/2020/> doi: 10.5194/gmd-13-1609-2020
- 471 Beauchamp, M., Febvre, Q., Georganos, H., & Fablet, R. (2022). 4DVarNet-
 472 SSH : end-to-end learning of variational interpolation schemes for nadir and
 473 wide-swath satellite altimetry. (November).
- 474 Bhattacharyya, A. (1943). On a measure of divergence between two statistical popu-
 475 lations defined by their probability distribution. *Bulletin of the Calcutta Math-
 476 ematical Society*, 35, 99–110.
- 477 Billett, D. S., Lampitt, R. S., Rice, A. L., & Mantoura, R. F. (1983). Seasonal sed-
 478 imentation of phytoplankton to the deep-sea benthos. *Nature*, 302(5908). doi:
 479 10.1038/302520a0
- 480 Bolton, T., & Zanna, L. (2019). Applications of Deep Learning to Ocean Data In-
 481 ference and Subgrid Parameterization. *Journal of Advances in Modeling Earth
 482 Systems*, 11(1). doi: 10.1029/2018MS001472
- 483 Breiman, L. (1996). Bagging predictors. *Machine Learning*, 24(2). doi: 10.1007/
 484 bf00058655

- Burd, A., Buchan, A., Church, M. J., Landry, M. R., McDonnell, A. M. P., Passow, U., ... Benway, H. M. (2016). *Towards a transformative understanding of the oceans biological pump: Priorities for future research - Report on the NSF Biology of the Biological Pump Workshop*. doi: 10.1575/1912/8263
- Burd, A. B., Hansell, D. A., Steinberg, D. K., Anderson, T. R., Arístegui, J., Baltar, F., ... Tanaka, T. (2010). Assessing the apparent imbalance between geochemical and biochemical indicators of meso- and bathypelagic biological activity: What the @\\$!is wrong with present calculations of carbon budgets? *Deep Sea Research Part II: Topical Studies in Oceanography*, 57(16), 1557–1571. Retrieved from <https://www.sciencedirect.com/science/article/pii/S0967064510000883> doi: <https://doi.org/10.1016/j.dsr2.2010.02.022>
- Cael, B. B., Cavan, E. L., & Britten, G. L. (2021, mar). Reconciling the Size-Dependence of Marine Particle Sinking Speed. *Geophysical Research Letters*, 48(5), e2020GL091771. Retrieved from <https://agupubs.onlinelibrary.wiley.com/doi/10.1029/2020GL091771> doi: 10.1029/2020GL091771
- Chapman, C., & Charantonis, A. A. (2017). Reconstruction of Subsurface Velocities From Satellite Observations Using Iterative Self-Organizing Maps. *IEEE Geoscience and Remote Sensing Letters*, 14(5). doi: 10.1109/LGRS.2017.2665603
- Chelton, D. B., Deszoeke, R. A., Schlax, M. G., El Naggar, K., & Siwertz, N. (1998). Geographical variability of the first baroclinic Rossby radius of deformation. *Journal of Physical Oceanography*, 28(3), 433–460. doi: 10.1175/1520-0485(1998)028<0433:GVOTFB>2.0.CO;2
- Cutolo, E., Pascual, A., Ruiz, S., Zarokanellos, N., & Fablet, R. (2022). CLOINet: Ocean state reconstructions through remote-sensing, in-situ sparse observations and Deep Learning. Retrieved from <http://arxiv.org/abs/2210.10767>
- Deuser, W. G., Muller-Karger, F. E., Evans, R. H., Brown, O. B., Esaias, W. E., & Feldman, G. C. (1990). Surface-ocean color and deep-ocean carbon flux: how close a connection? *Deep Sea Research Part A, Oceanographic Research Papers*, 37(8). doi: 10.1016/0198-0149(90)90046-X
- Deuser, W. G., Muller-Karger, F. E., & Hemleben, C. (1988). Temporal variations of particle fluxes in the deep subtropical and tropical North Atlantic: Eulerian versus Lagrangian effects. *Journal of Geophysical Research*, 93(C6). doi: 10.1029/JC093iC06p06857
- Deuser, W. G., & Ross, E. H. (1980). *Seasonal change in the flux of organic carbon to the deep Sargasso Sea [5]* (Vol. 283) (No. 5745). doi: 10.1038/283364a0
- Dever, M., Nicholson, D., Omand, M. M., & Mahadevan, A. (2021, mar). Size-Differentiated Export Flux in Different Dynamical Regimes in the Ocean. *Global Biogeochemical Cycles*, 35(3), e2020GB006764. Retrieved from <https://onlinelibrary.wiley.com/doi/10.1029/2020GB006764> doi: 10.1029/2020GB006764
- Dunne, J. P., Armstrong, R. A., Gnanadesikan, A., & Sarmiento, J. L. (2005, dec). Empirical and mechanistic models for the particle export ratio. *Global Biogeochemical Cycles*, 19(4). Retrieved from <https://agupubs.onlinelibrary.wiley.com/doi/10.1029/2004GB002390> doi: 10.1029/2004GB002390
- Frigstad, H., Henson, S. A., Hartman, S. E., Omar, A. M., Jeansson, E., Cole, H., ... Lampitt, R. S. (2015, oct). Links between surface productivity and deep ocean particle flux at the Porcupine Abyssal Plain sustained observatory. *Biogeosciences*, 12(19), 5885–5897. doi: 10.5194/bg-12-5885-2015
- George, T. M., Manucharyan, G. E., & Thompson, A. F. (2021). Deep learning to infer eddy heat fluxes from sea surface height patterns of mesoscale turbulence. *Nature Communications*, 12(1). doi: 10.1038/s41467-020-20779-9
- Gula, J., & Collin, J. (2021, June). *Pyicles: a Python/Fortran hybrid parallelized code for 3D Lagrangian particles advection using ROMS/CROCO model data*. Zenodo. Retrieved from <https://doi.org/10.5281/zenodo.4973786> doi: 10.5281/zenodo.4973786

- 541 Hartman, S. E., Bett, B. J., Durden, J. M., Henson, S. A., Iversen, M., Jeffreys,
 542 R. M., ... Gates, A. R. (2021, feb). Enduring science: Three decades of
 543 observing the Northeast Atlantic from the Porcupine Abyssal Plain Sus-
 544 tained Observatory (PAP-SO). *Progress in Oceanography*, 191, 102508.
 545 Retrieved from [https://linkinghub.elsevier.com/retrieve/pii/
 546 S0079661120302433](https://linkinghub.elsevier.com/retrieve/pii/S0079661120302433) doi: 10.1016/j.pocean.2020.102508
- 547 Haynes, K., Lagerquist, R., McGraw, M., Musgrave, K., & Ebert-Uphoff, I. (2023).
 548 Creating and Evaluating Uncertainty Estimates with Neural Networks for
 549 Environmental-Science Applications. *Artificial Intelligence for the Earth Sys-
 550 tems*, 2(2), 1–29. doi: 10.1175/aies-d-22-0061.1
- 551 Henson, S. A., Laufkötter, C., Leung, S., Giering, S. L., Palevsky, H. I., & Ca-
 552 van, E. L. (2022, apr). Uncertain response of ocean biological carbon
 553 export in a changing world. *Nature Geoscience*, 15(4), 248–254. doi:
 554 10.1038/s41561-022-00927-0
- 555 Iversen, M. H., & Lampitt, R. S. (2020, nov). Size does not matter after all: No ev-
 556 idence for a size-sinking relationship for marine snow. *Progress in Oceanogra-
 557 phy*, 189, 102445. doi: 10.1016/j.pocean.2020.102445
- 558 Jenkins, J., Paiement, A., Ourmières, Y., Sommer, J. L., Verron, J., Ubelmann, C.,
 559 & Glotin, H. (2022). A DNN Framework for Learning Lagrangian Drift With
 560 Uncertainty. Retrieved from <http://arxiv.org/abs/2204.05891>
- 561 Jokulsdottir, T., & Archer, D. (2016, apr). A stochastic, Lagrangian model of
 562 sinking biogenic aggregates in the ocean (SLAMS 1.0): Model formulation,
 563 validation and sensitivity. *Geoscientific Model Development*, 9(4), 1455–1476.
 564 doi: 10.5194/gmd-9-1455-2016
- 565 Kingma, D. P., & Ba, J. L. (2015). Adam: A method for stochastic optimization. In
 566 *3rd international conference on learning representations, iclr 2015 - conference
 567 track proceedings*.
- 568 Kostadinov, T. S., Siegel, D. A., & Maritorena, S. (2009, sep). Retrieval of the
 569 particle size distribution from satellite ocean color observations. *Jour-
 570 nal of Geophysical Research: Oceans*, 114(C9). Retrieved from <https://agupubs.onlinelibrary.wiley.com/doi/10.1029/2009JC005303> doi:
 572 10.1029/2009JC005303
- 573 Lampitt, R. S., Achterberg, E. P., Anderson, T. R., Hughes, J. A., Iglesias-
 574 Rodriguez, M. D., Kelly-Gerreyn, B. A., ... Yool, A. (2008). Ocean fertil-
 575 ization: A potential means of geoengineering? *Philosophical Transactions
 576 of the Royal Society A: Mathematical, Physical and Engineering Sciences*,
 577 366(1882). doi: 10.1098/rsta.2008.0139
- 578 Lampitt, R. S., Briggs, N., Cael, B. B., Espinola, B., Hélaouët, P., Henson, S. A.,
 579 ... Smeed, D. (2023, oct). Deep ocean particle flux in the Northeast At-
 580 lantic over the past 30 years: carbon sequestration is controlled by ecosystem
 581 structure in the upper ocean. *Frontiers in Earth Science*, 11, 1176196. doi:
 582 10.3389/feart.2023.1176196
- 583 Laurenceau-Cornec, E. C., Le Moigne, F. A. C., Gallinari, M., Moriceau, B., Toul-
 584 lec, J., Iversen, M. H., ... De La Rocha, C. L. (2020, jun). New guidelines
 585 for the application of Stokes' models to the sinking velocity of marine ag-
 586 ggregates. *Limnology and Oceanography*, 65(6), 1264–1285. Retrieved from
 587 <https://aslopubs.onlinelibrary.wiley.com/doi/10.1002/lno.11388>
 588 doi: 10.1002/lno.11388
- 589 Le Cann, B. (2005, jul). Observed mean and mesoscale upper ocean circulation in
 590 the midlatitude northeast Atlantic. *Journal of Geophysical Research*, 110(C7),
 591 C07S05. Retrieved from <http://doi.wiley.com/10.1029/2004JC002768> doi:
 592 10.1029/2004JC002768
- 593 Le Corre, M., Gula, J., & Tréguier, A. M. (2020, apr). Barotropic vorticity bal-
 594 ance of the North Atlantic subpolar gyre in an eddy-resolving model. *Ocean
 595 Science*, 16(2), 451–468. doi: 10.5194/os-16-451-2020

- 596 Le Moigne, F. A., Henson, S. A., Sanders, R. J., & Madsen, E. (2013, aug). Global
 597 database of surface ocean particulate organic carbon export fluxes diagnosed
 598 from the ^{234}Th technique. *Earth System Science Data*, 5(2), 295–304. doi:
 599 10.5194/essd-5-295-2013
- 600 Le Moigne, F. A. C. (2019, oct). Pathways of Organic Carbon Downward Trans-
 601 port by the Oceanic Biological Carbon Pump. *Frontiers in Marine Science*, 6,
 602 482488. Retrieved from [https://www.frontiersin.org/article/10.3389/fmars.2019.00634](https://www.frontiersin.org/article/10.3389/fmars.2019.00634/full) doi: 10.3389/fmars.2019.00634
- 603 Lecun, Y., Bengio, Y., & Hinton, G. (2015). Deep learning. *Nature*, 521(7553), 436–
 604 444. doi: 10.1038/nature14539
- 605 Liu, G., Bracco, A., & Passow, U. (2018, jan). The influence of mesoscale and sub-
 606 mesoscale circulation on sinking particles in the northern Gulf of Mexico. *Ele-
 607 mента*, 6. doi: 10.1525/elementa.292
- 608 Ma, W., Xiu, P., Chai, F., Ran, L., Wiesner, M. G., Xi, J., ... Fredj, E. (2021). Impact of mesoscale eddies on the source funnel of sediment trap measurements in the South China Sea. *Progress in Oceanography*, 194, 102566. Retrieved from <https://doi.org/10.1016/j.pocean.2021.102566> doi: 10.1016/j.pocean.2021.102566
- 609 Manucharyan, G. E., Siegelman, L., & Klein, P. (2021). A Deep Learning Approach
 610 to Spatiotemporal Sea Surface Height Interpolation and Estimation of Deep
 611 Currents in Geostrophic Ocean Turbulence. *Journal of Advances in Modeling
 612 Earth Systems*, 13(1), 1–17. doi: 10.1029/2019MS001965
- 613 Passow, U., & Carlson, C. A. (2012). The biological pump in a high CO₂ world. *Marine Ecology Progress Series*, 470. doi: 10.3354/meps09985
- 614 Paszke, A., Gross, S., Massa, F., Lerer, A., Bradbury, J., Chanan, G., ... Chintala,
 615 S. (2019). Pytorch: An imperative style, high-performance deep learning
 616 library. In *Advances in neural information processing systems 32* (pp. 8024–
 617 8035). Curran Associates, Inc. Retrieved from <http://papers.neurips.cc/paper/9015-pytorch-an-imperative-style-high-performance-deep-learning-library.pdf>
- 618 Pauthenet, E., Bachelot, L., Balem, K., Maze, G., Tréguier, A. M., Roquet, F., ...
 619 Tandeo, P. (2022). Four-dimensional temperature, salinity and mixed-
 620 layer depth in the Gulf Stream, reconstructed from remote-sensing and in situ
 621 observations with neural networks. *Ocean Science*, 18(4), 1221–1244. doi:
 622 10.5194/os-18-1221-2022
- 623 Rembauville, M., Blain, S., Manno, C., Tarling, G., Thompson, A., Wolff, G., &
 624 Salter, I. (2018). The role of diatom resting spores in pelagic-benthic coupling
 625 in the Southern Ocean. *Biogeosciences*, 15(10). doi: 10.5194/bg-15-3071-2018
- 626 Ronneberger, O., Fischer, P., & Brox, T. (2015, may). U-Net: Convolu-
 627 tional Networks for Biomedical Image Segmentation. Retrieved from
 628 <http://arxiv.org/abs/1505.04597>
- 629 Shchepetkin, A. F., & McWilliams, J. C. (2005). The regional oceanic modeling
 630 system (ROMS): A split-explicit, free-surface, topography-following-coordinate
 631 oceanic model. *Ocean Modelling*, 9(4). doi: 10.1016/j.ocemod.2004.08.002
- 632 Siegel, D. A., Buesseler, K. O., Doney, S. C., Sailley, S. F., Behrenfeld, M. J., &
 633 Boyd, P. W. (2014). Global assessment of ocean carbon export by com-
 634 bining satellite observations and food-web models. *Global Biogeochemical
 635 Cycles*, 28(3), 181–196. Retrieved from <https://agupubs.onlinelibrary.wiley.com/doi/abs/10.1002/2013GB004743> doi: <https://doi.org/10.1002/2013GB004743>
- 636 Siegel, D. A., Fields, E., & Buesseler, K. O. (2008). A bottom-up view of the biolog-
 637 ical pump: Modeling source funnels above ocean sediment traps. *Deep-Sea Re-
 638 search Part I: Oceanographic Research Papers*, 55(1). doi: 10.1016/j.dsr.2007
 639 .10.006
- 640 Siegel, D. A., Granata, T. C., Michaels, A. F., & Dickey, T. D. (1990). Mesoscale

- 651 eddy diffusion, particle sinking, and the interpretation of sediment trap data.
652 *Journal of Geophysical Research*, 95(C4). doi: 10.1029/JC095iC04p05305
- 653 Turner, J. T. (2015, jan). *Zooplankton fecal pellets, marine snow, phytodetritus and*
654 *the ocean's biological pump* (Vol. 130). Elsevier Ltd. doi: 10.1016/j.pocean.2014
655 .08.005
- 656 Villa-Alfageme, M., de Soto, F. C., Ceballos, E., Giering, S. L. C., Le Moigne,
657 F. A. C., Henson, S., ... Sanders, R. J. (2016, aug). Geographical, sea-
658 sonal, and depth variation in sinking particle speeds in the North Atlantic.
659 *Geophysical Research Letters*, 43(16), 8609–8616. Retrieved from <http://doi.wiley.com/10.1002/2016GL069233> doi: 10.1002/2016GL069233
- 660 Wang, L., Gula, J., Collin, J., & Mémery, L. (2022). Effects of Mesoscale Dy-
661 namics on the Path of Fast-Sinking Particles to the Deep Ocean: A Mod-
662 eling Study. *Journal of Geophysical Research: Oceans*, 127(7), 1–30. doi:
663 10.1029/2022JC018799
- 664 Wekerle, C., Krumpen, T., Dinter, T., von Appen, W. J., Iversen, M. H., & Salter,
665 I. (2018). Properties of sediment trap catchment areas in fram strait: Results
666 from Lagrangian modeling and remote sensing. *Frontiers in Marine Science*,
667 9(NOV). doi: 10.3389/fmars.2018.00407
- 668 Williams, R. G., & Follows, M. J. (2011). *Ocean dynamics and the carbon*
669 *cycle: Principles and mechanisms.* Cambridge University Press. doi:
670 10.1017/CBO9780511977817
- 671